Report

Neuron

Topographic Mapping of the Synaptic Cleft into Adhesive Nanodomains

Highlights

- A macromolecular definition is given for synaptic cleft organization
- SynCAM 1 shapes the cleft edge, while EphB2 is enriched deeper postsynaptically
- *Trans*-synaptic complexes can assemble into cloud-like ensembles at the synaptic edge
- Synaptic adhesion complexes undergo dynamic, activity-dependent redistribution

Authors

Karen Perez de Arce, Nikolas Schrod, Sarah W.R. Metzbower, ..., Thomas A. Blanpied, Vladan Lučić, Thomas Biederer

Correspondence

thomas.biederer@tufts.edu

In Brief

Perez de Arce et al. show that the cleft of excitatory synapses is composed of structurally and molecularly defined sub-compartments, the cleft is dynamic, and *trans*-synaptic interactions shape the cleft's edge. These findings bring the concept of nanodomains to the cleft.

Perez de Arce et al., 2015, Neuron *88*, 1165–1172
December 16, 2015
http://dx.doi.org/10.1016/j.neuron.2015.11.011

CellPress

Neuron
Report

Topographic Mapping of the Synaptic Cleft into Adhesive Nanodomains

Karen Perez de Arce,[1] Nikolas Schrod,[2] Sarah W.R. Metzbower,[3] Edward Allgeyer,[4] Geoffrey K.-W. Kong,[2,6] Ai-Hui Tang,[3] Alexander J. Krupp,[5] Valentin Stein,[5] Xinran Liu,[4] Jörg Bewersdorf,[4] Thomas A. Blanpied,[3] Vladan Lučić,[2] and Thomas Biederer[1,*]

[1]Department of Neuroscience, Tufts University School of Medicine, Boston, MA 02111, USA
[2]Department of Molecular Structural Biology, Max Planck Institute of Biochemistry, 82152 Martinsried, Germany
[3]Department of Physiology, University of Maryland School of Medicine, Baltimore, MD 21201, USA
[4]Department of Cell Biology, Yale University School of Medicine, New Haven, CT 06520, USA
[5]Department of Physiology, Universität Bonn Medical Faculty, 53115 Bonn, Germany
[6]Present address: Plant Molecular Biology Laboratory, University of Hong Kong, Hong Kong, PRC
*Correspondence: thomas.biederer@tufts.edu
http://dx.doi.org/10.1016/j.neuron.2015.11.011

SUMMARY

The cleft is an integral part of synapses, yet its macromolecular organization remains unclear. We show here that the cleft of excitatory synapses exhibits a distinct density profile as measured by cryo-electron tomography (cryo-ET). Aiming for molecular insights, we analyzed the synapse-organizing proteins Synaptic Cell Adhesion Molecule 1 (SynCAM 1) and EphB2. Cryo-ET of SynCAM 1 knockout and overexpressor synapses showed that this immunoglobulin protein shapes the cleft's edge. SynCAM 1 delineates the postsynaptic perimeter as determined by immunoelectron microscopy and super-resolution imaging. In contrast, the EphB2 receptor tyrosine kinase is enriched deeper within the postsynaptic area. Unexpectedly, SynCAM 1 can form ensembles proximal to postsynaptic densities, and synapses containing these ensembles were larger. Postsynaptic SynCAM 1 surface puncta were not static but became enlarged after a long-term depression paradigm. These results support that the synaptic cleft is organized on a nanoscale into sub-compartments marked by distinct *trans*-synaptic complexes.

INTRODUCTION

Neuronal transmission requires precise organization of pre- and postsynaptic specializations (Harris and Weinberg, 2012; Sigrist and Sabatini, 2012). Limited structural insights are available into the synaptic cleft, the third compartment of a synapse. Current results show that the complexes spanning the cleft form net-like structures that can be periodically arranged (Lučić et al., 2005; Zuber et al., 2005; High et al., 2015).

Trans-synaptic interactions modulate synapse development and plasticity (Missler et al., 2012). Ultrastructural localization of N-cadherin shows that it is expressed throughout the cleft of developing synapses and present at the edge of mature synapses (Elste and Benson, 2006; Uchida et al., 1996; Yamagata et al., 1995). N-cadherin does not induce synapses, and comparable insights into synaptogenic proteins are lacking, though immunoelectron microscopy (immuno-EM) studies have demonstrated the differential expression of neuroligins at excitatory and inhibitory synapses (Song et al., 1999; Varoqueaux et al., 2004; Mortillo et al., 2012). Synaptogenic proteins may demarcate and function at specialized synaptic zones, yet limited understanding of cleft topography restricts addressing these questions.

We here delineated macromolecular properties of the excitatory synaptic cleft. To gain molecular insights, we investigated two proteins that form *trans*-synaptic complexes to promote excitatory synapse number, the immunoglobulin adhesion protein SynCAM 1 (Synaptic Cell Adhesion Molecule 1, also named nectin-like 2 or Cadm1) (Biederer et al., 2002; Fogel et al., 2007; Robbins et al., 2010) and the EphB2 receptor tyrosine kinase (Sheffler-Collins and Dalva, 2012). Analysis of excitatory synapses by cryoelectron tomography (cryo-ET), immuno-EM, and STED (stimulated emission depletion) and STORM (stochastic optical reconstruction microscopy) super-resolution imaging supports that the synaptic cleft is composed of structurally and molecularly defined sub-compartments.

RESULTS

Structural Organization of the Cleft of Excitatory Synapses

Cryo-ET enables high-resolution imaging of the entire cleft in a fully hydrated, physiologically relevant state (Lučič et al., 2013). We recorded tomograms of neocortical synaptosomes from adult mice (Figures 1A and S1A). All analyzed synapses were asymmetric with a postsynaptic density (PSD) and likely corresponded to excitatory synapses. The mean cleft width of wild-type (WT) synapses was 22.0 ± 0.5 nm (Figure S1C), as described (Rees et al., 1976). Numerous complexes spanned the cleft and often assumed the shape of a laterally extended, net-like density (Figure 1A; Movie S1), as described (Lučić

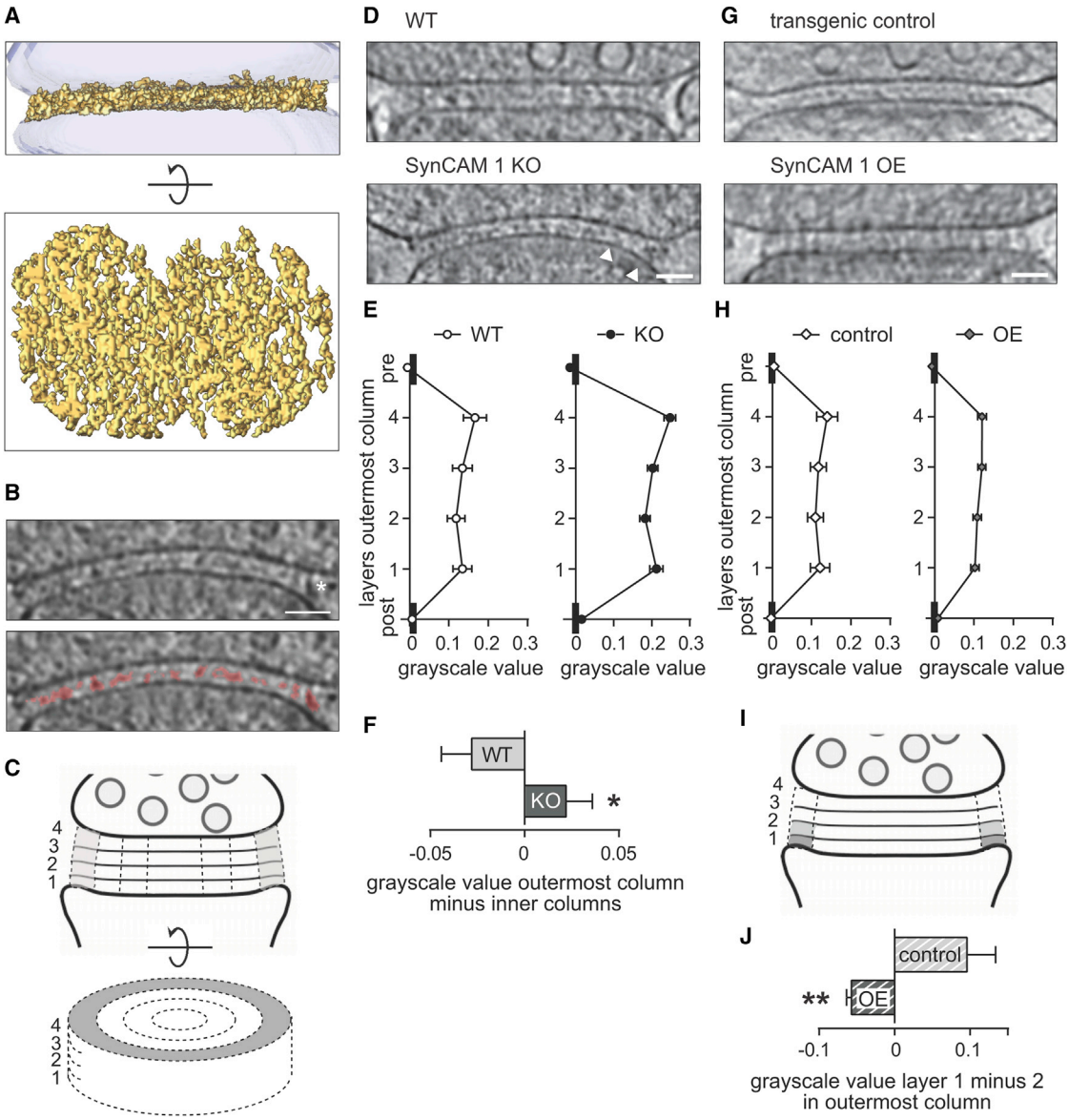

Figure 1. The Excitatory Synaptic Cleft Is Structurally Organized and SynCAM 1 Shapes the Edge

(A) Top: side view of a segmented synaptic cleft. Bottom: top view.

(B) Top: tomographic slice from a synaptosome at a 4 voxel depth (9.2 nm). Bottom: segmented net-like structures closer to the postsynaptic (lower) side are marked in red. The asterisk marks a gold particle for tomogram alignment. Scale bar, 50 nm.

(C) Cleft separation into four layers and concentric columns. The outermost column is shown in gray.

(D) WT and SynCAM 1 KO cleft tomograms at a 4 voxel depth (9.2 nm). Arrowheads mark the less dense central density toward the edge of the KO cleft. Scale bar, 50 nm.

(E) Profiles of the outermost WT and KO cleft columns. Lower grayscale values correspond to higher densities. Mean layer values were calculated in each tomogram and averaged per genotype (N = 7 WT, 8 KO synapses).

(F) SynCAM 1 KO synapses have a higher grayscale value differential and hence a lower relative protein density in the outer column compared to the inner columns (N = 7 WT, 8 KO synapses). Error bars, SEM; unpaired t-test.

(G) Tomograms of transgenic control and SynCAM 1 OE clefts at a 4 voxel depth (9.2 nm). The central cleft density of the control is barely visible in OE synapses. Scale bar, 50 nm.

(H) Flat profile of the SynCAM 1 OE cleft. Grayscale values are shown as in (E) (N = 5 synapses each).

(I) Data in (J) was calculated by subtracting grayscale values of volumes depicted in light gray from those in dark gray.

(J) SynCAM 1 OE synapses have higher protein density in layer 1 relative to layer 2 in the outer cleft column compared to controls (N = 5 synapses each). Error bars, SEM; unpaired t-test.

See also Figure S1 and Movies S1 and S2.

et al., 2005). *Trans* complexes and net-like structures were seen in all analyzed tomograms.

Observation of tomograms indicated an increased central density in the cleft, closer to the postsynaptic side (Figure 1B; Movie S2). To measure whether this density is offset from the middle, we separated the cleft into four layers because this gave the most robust results with low noise (Figure 1C). Each cleft was further divided into four concentric columns with even radii (Figure 1C). Lower cryo-ET grayscale values correspond to higher protein densities, and mean grayscale values exhibited a minimum, i.e., highest, density in the second layer counted from the post- to pre-synaptic membrane when all columns were combined (layer 2 versus layers 1, 3, 4; paired t test, $p = 0.0007$ [layer 1], $p = 0.015$ [layer 3], $p = 0.0001$ [layer 4]; $N = 7$ WT synapses), as well as in the outermost column (Figures 1D and 1E, left; layer 2 versus layers 1, 3, 4; paired t test, $p = 0.015$ [layer 1], $p = 0.019$ [layer 3], $p = 0.0003$ [layer 4]; $N = 7$ WT synapses). Densities of the four cleft columns were indistinguishable (data not shown).

The Edge of the Synaptic Cleft is Shaped by SynCAM 1

We next tested whether SynCAM 1 affects the makeup of the synaptic cleft, choosing this immunoglobulin adhesion protein due to its expression across excitatory forebrain synapses, its ability to increase excitatory synapse number in cultured neurons and the brain, and the high synaptic membrane content of SynCAMs (Biederer et al., 2002; Fogel et al., 2007; Robbins et al., 2010). Neocortical synaptosomes from adult SynCAM 1 knockout (KO) mice had the same cleft width as those from WT (Figures 1D, S1A, and S1C). Loss of SynCAM 1 did not alter the layer profile when the data of all columns were averaged (data not shown) or in the outermost column (Figures 1D and 1E, right). The higher grayscale values in the KO could not be interpreted with certainty as lower total cleft protein amounts because of the inability to determine absolute values with cryo-ET. However, relative changes can be robustly compared. This showed that synapses lacking SynCAM 1 exhibited a loss of relative protein density, i.e., an increased grayscale differential, in the outermost cleft column compared to the inner columns (Figure 1F; t test, $p = 0.037$; $N = 7$ WT and 8 KO synapses). Loss of SynCAM 1 therefore lowers the density distribution toward the synaptic edge.

Because SynCAM 1 loss preserved the highest density in layer 2, other complexes likely establish this profile. We asked whether those interactions can be imbalanced by elevating SynCAM 1. We recorded cryo-ET images of synaptosomes from transgenic mice overexpressing SynCAM 1 in excitatory neurons and from littermates lacking the SynCAM 1 transgene (transgenic controls) (Figure 1G). Cleft width was unaffected by elevated SynCAM 1 (Figures S1B and S1C). Control synapses showed the layer profile expected from WT synapses (Figure 1H, left, versus Figure 1E, left). In contrast, the profile of overexpressor (OE) synapses was flat (Figure 1H, right). We measured an inverted difference (higher density in layer 1 than in layer 2) in the outermost column of OE synapses, different from controls (t test, $p = 0.0044$; $N = 5$ synapses each) (Figures 1I and 1J). This inversion only occurred in the outermost column (data not shown). Elevated SynCAM 1 therefore disrupts the layer profile in the outer cleft column, possibly through its increased expression at the postsynaptic edge. These structural aberrations after loss and overexpression of SynCAM 1 indicated that this adhesion protein organizes the outer zone of the cleft.

SynCAM 1 Localizes to the Postsynaptic Edge of Excitatory Synapses

We next localized endogenous SynCAM 1 using immuno-EM of high-pressure frozen hippocampal slices from adult mice (Figure 2A). In CA1 stratum radiatum, anti-SynCAM 1 immunogold particles labeled most frequently excitatory synapses. This was expected from an immuno-EM study with antibodies detecting the family members SynCAM 1, 2, or 3 equally well (Biederer et al., 2002) and biochemical fractionation (Fogel et al., 2007). Synaptic labeling was reduced by 84% ± 4% in SynCAM 1 KO sections, validating antibody specificity (Figure S2A). At WT CA1 synapses, gold particles were most common at postsynaptic membranes (46% ± 6% of total synaptic labeling) (Figure 2B). Less labeling was found in the pre- and postsynaptic cytomatrix and presynaptic membranes. To map SynCAM 1 distribution, we measured distances of the gold particles at postsynaptic membranes relative to the PSD center (Figure 2C). This determined that postsynaptic SynCAM 1 localizes to the cleft edge (Figure 2D). The less abundant SynCAM 1 particles at presynaptic membranes were distributed as two populations, one more central and the other peri-synaptic (Figure S2B). These results supported an enrichment of postsynaptic SynCAM 1 at the edge of excitatory synapses.

EphB2 and SynCAM 1 Complexes Mark Distinct Sub-synaptic Areas

A second important player in the cleft is the postsynaptic receptor tyrosine kinase EphB2 that promotes excitatory synaptogenesis during the rapid phase of synapse addition before neurons mature (Kayser et al., 2008; Sheffler-Collins and Dalva, 2012). This role differs from SynCAM 1, which first induces and then maintains excitatory synapses (Robbins et al., 2010). We speculated that this functional difference may be reflected in distinct sub-synaptic localizations. We first addressed to what extent these proteins co-localize at excitatory synapses. Non-permeabilized hippocampal neurons were immunolabeled for endogenous, surface-expressed SynCAM 1 and EphB2 at 14 days in vitro (div) with antibodies against their extracellular domains, followed by permeabilization, immunostaining for the excitatory postsynaptic scaffold protein Homer, and confocal microscopy (Figure 2E). SynCAM 1 and EphB2 were detected at comparable densities along dendrites (data not shown). Automated three-channel co-localization analysis measured that 74% ± 9% of Homer puncta contained SynCAM 1, EphB2, or both. Of the Homer-positive SynCAM 1 puncta, 88% ± 1% co-localized with EphB2, while all synaptic EphB2 puncta were positive for SynCAM 1 ($N = 69$ dendritic segments from three independent experiments).

We next analyzed the sub-synaptic distribution of surface SynCAM 1 and EphB2 by two-channel STED super-resolution microscopy, applying the same sequential immunostaining (Figures 2F and 2G). This showed that SynCAM 1 has a high density at the PSD border, while EphB2 resides within the bounds of the

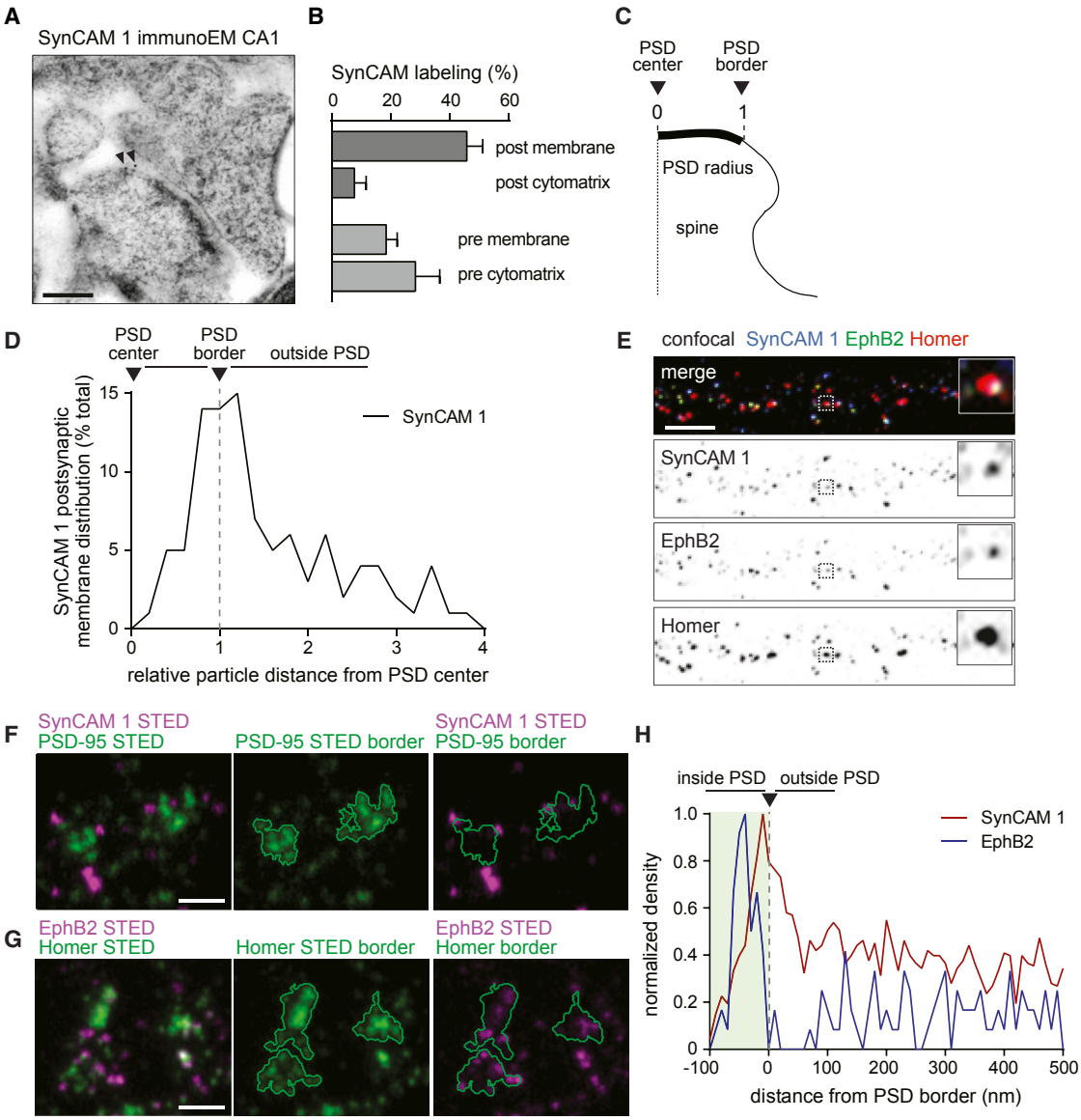

Figure 2. Postsynaptic SynCAM 1 Marks the Perimeter of Excitatory Synapses and EphB2 Is Enriched Deeper within the Postsynaptic Area

(A) Immuno-EM of SynCAM 1 in the adult hippocampal CA1 area after high-pressure freezing. Arrows mark 10 nm gold particles labeling SynCAM 1 at the postsynaptic membrane edge of an asymmetric synapse.

(B) A majority of synaptic SynCAM 1 localizes to postsynaptic membranes (N = 97 micrographs, 3 mice).

(C) Measurement of postsynaptic distances for quantification in (D), where 0 marks the PSD center and 1 marks the edge.

(D) Postsynaptic membrane SynCAM 1 is enriched at the PSD edge. Particle distances to the PSD center were measured for each synapse and normalized as in (C) (N = 97 micrographs, 3 mice).

(E) Hippocampal neurons were sequentially immunostained at 14 div to first detect surface SynCAM 1 (blue) and surface EphB2 (green), followed by permeabilization and staining for postsynaptic Homer (red) and confocal imaging. Each box marks the synapse enlarged in the inset. Scale bar, 5 μm.

(F and G) Hippocampal neurons at 14 div were subjected to sequential immunostaining for (F) surface SynCAM 1 (magenta) and PSD-95 (green) or (G) surface EphB2 (magenta) and Homer (green) and were imaged by two-color STED microscopy. PSD borders based on STED image analysis are shown in the center and right panels. Scale bars, 400 nm.

(H) Surface SynCAM 1 and EphB2 locations were determined by STED as in (F) and (G), and distances were measured from the PSD border defined by PSD-95 and Homer images, respectively. SynCAM 1 (red) reached maximum density at the PSD border (green). EphB2 (blue) was prominently located within PSD areas. Densities were normalized to the highest value. SynCAM 1 data are from 696 PSD areas in 86 imaging fields; EphB2 data are from 111 PSD areas in 10 fields. See also Figure S2.

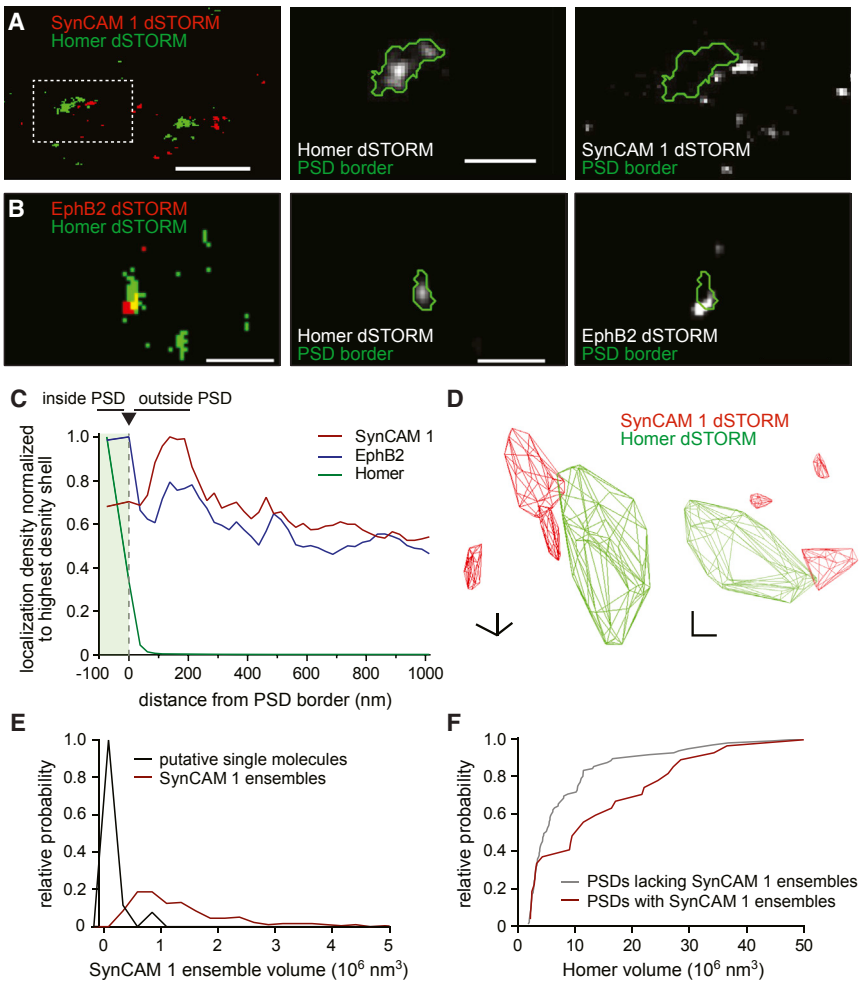

Figure 3. Distinct 3D Distribution of EphB2 and SynCAM 1 and Presence of SynCAM 1 Ensembles around the Cleft

(A and B) Left: hippocampal neurons at 12–14 div were subjected to sequential immunostaining for surface SynCAM 1 (A) or EphB2 (B) (red) and intracellular Homer (green) and imaged by two-channel 3D STORM. Center and right: enlarged PSD with the calculated border outlined. Scale bar overview, 1 μm; enlarged panels, 400 nm.

(C) Surface SynCAM 1 and EphB2 localizations were determined by 3D STORM as in (A) and (B), and the PSD border was defined by super-resolved Homer localizations. SynCAM 1 localization density (red) reached a maximum around the PSD edge (green), and localizations within Homer hulls (green) were rare. EphB2 (blue) was prominently localized within the area demarcated by the PSD and showed a smaller peak around the edge. SynCAM 1 data from 178 PSDs in 11 imaging fields; EphB2 data from 446 PSDs in 31 fields.

(D) Two 3D views of a convex, Homer-defined PSD hull (green; boxed in A) showing adjacent ensembles of SynCAM 1 (red). Scale bars, 200 nm in each axis.

(E) Distribution of SynCAM 1 ensemble volumes within 500 nm of a PSD. Gray shows putative single molecules detected at low thresholds. Red shows ensembles detected at a threshold excluding single molecules.

(F) PSDs marked by SynCAM 1 ensembles are larger. Cumulative frequency distribution of super-resolved Homer volumes in spines lacking SynCAM 1 ensembles (gray) or containing at least one SynCAM 1 ensemble (red) within 500 nm of the Homer hull. Ensembles were identified as in (E) (N = 120 PSDs lacking SynCAM 1 ensembles, 31 PSDs with ensembles from 11 fields of imaging; Mann-Whitney test, $p = 0.026$).

See also Figure S3.

PSD proper (Figure 2H). *Trans*-synaptic complexes can therefore mark distinct synaptic zones.

3D Localization Shows Differential EphB2 and SynCAM Distribution and Reveals Cloud-like SynCAM Ensembles

What is the three-dimensional (3D) distribution of synapse-organizing proteins? To address this question, we used two-color 3D direct STORM (Huang et al., 2008) to analyze cultures of hippocampal neurons at 12–14 div. Endogenous, surface-expressed SynCAM 1 or EphB2 and postsynaptic Homer were visualized by sequential immunostaining and imaged by 3D direct STORM (Figures 3A and 3B). SynCAM 1 and EphB2 were found along dendrites, including near Homer-positive PSDs. The 3D border of each PSD was defined with a convex hull around Homer localizations (Dani et al., 2010; MacGillavry et al., 2013), and the density of SynCAM localizations was determined within this border and outside it in 50 nm shells (Figure 3C). This revealed a prominent peak of SynCAM 1 density between 100 and 200 nm outside the PSD border. This agrees with the immuno-EM and STED localizations, though differences of synapses formed in vivo and by cultured neurons, maturation stage, and two-dimensional STED and 3D STORM imaging need to be considered. We consider antibody penetration issues unlikely, because post-embedding immuno-EM, which is not expected to be affected by access issues, showed similarly restricted labeling (Figure 2D). In contrast to SynCAM 1, EphB2 localizations by 3D STORM were most prominent deeper within the postsynaptic area, with a smaller peak of EphB2 between 100 and 200 nm outside the PSD (Figures 3B and 3C).

Of all PSDs, 79% had SynCAM surface localizations within 500 nm of their border and a subset of SynCAM 1 localizations appeared in large ensembles (Figure 3D). To characterize these grouped localizations using automated analysis, we applied area and density criteria to select ensembles that likely consisted of multiple SynCAM 1 molecules (Figures 3E and S3). The volume of SynCAM 1 ensembles varied widely, averaging 8.4 x 10^6 nm^3 with a SD of 6.6 x 10^6 nm^3. The median volume was 3.9 x 10^6 nm^3, approximately one-third the volume of Homer-defined PSDs (median 9.4 x 10^6 ± 1.5 x 10^6 nm^3). Of PSDs, 21% had SynCAM 1 ensembles within 500 nm of their border, suggesting that they belonged to a unique subpopulation of synapses. To determine whether the presence of SynCAM 1 ensembles

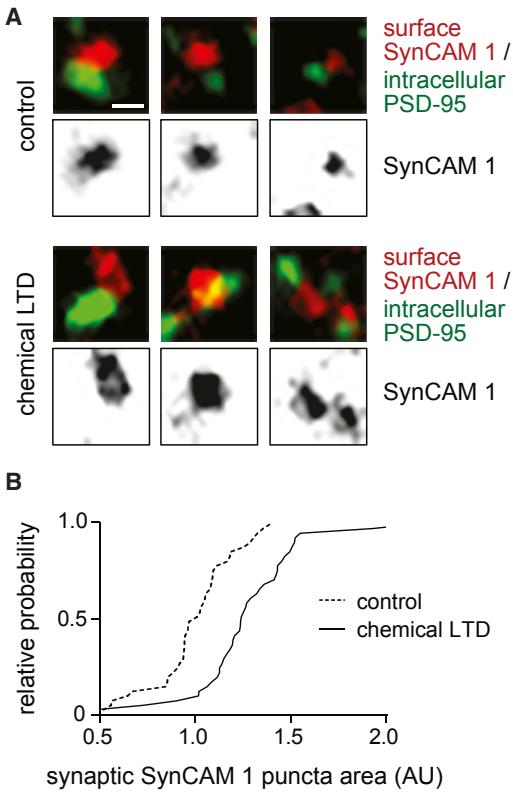

Figure 4. Activity-Dependent Area Changes of Synaptic SynCAM 1 Complexes

(A) Hippocampal neurons at 14 div were subjected to chemical LTD. Surface SynCAM 1 was immunolabeled (red), followed by staining for postsynaptic PSD-95 (green) and confocal imaging. Three representative images show control synapses (top) or synapses after chemical LTD treatment (bottom). Scale bar, 0.8 μm.

(B) LTD treatment enlarges the area of synaptic SynCAM 1 puncta. The graph shows the cumulative frequency distribution of SynCAM 1 punctum areas located within 0.8 μm of a PSD-95 punctum (Mann-Whitney test, $p < 0.0001$; N = 41 neurites each).

correlated with structural features, we measured Homer clusters (Figure 3F). This showed that synapses lacking SynCAM 1 ensembles had an average Homer volume of $7.2 \times 10^6 \pm 0.8 \times 10^6$ nm^3 (N = 120), while Homer clusters had almost twice the volume when marked by SynCAM 1 ensembles ($13.1 \times 10^6 \pm 2.3 \times 10^6$ nm^3; N = 31; t test, p = 0.003). These ensembles thus revealed a novel macromolecular feature of *trans*-synaptic complexes.

The Synaptic Cleft Is a Dynamic Compartment

Neuronal activity and synaptic plasticity regulate the trafficking of N-cadherin and its interactions with β-catenins (Hirano and Takeichi, 2012). Can the distribution of synaptogenic proteins also change in an activity-dependent manner? SynCAM 1 was well suited to test this question, because the position of SynCAM complexes at the synaptic edge may allow them to be readily dispersed. We used a chemical long-term depression (LTD) protocol because SynCAM 1 regulates LTD in vivo (Robbins et al., 2010). Sequential immunostainings were performed for surface SynCAM 1 and the excitatory postsynaptic scaffold protein PSD-95 and were imaged by confocal microscopy (Figure 4A). Analysis was restricted to surface-labeled SynCAM 1 within 0.8 μm of the center of the nearest PSD-95 punctum to measure SynCAM 1 puncta within approximately one PSD diameter, which in our confocal analysis was 0.65 ± 0.02 μm (N = 41 neurites). LTD treatment enlarged synaptic SynCAM 1 puncta by 27% ± 5% (t test, $p < 0.0001$; N = 41 neurites each). Frequency distribution analysis supported a LTD-induced enlargement of SynCAM 1 puncta across all area ranges (Figure 4B). Synaptic SynCAM 1 proteins can therefore undergo dynamic changes in their surface distribution.

DISCUSSION

This study reports five findings about the cleft of excitatory synapses. First, the cleft is structurally patterned. Second, the cleft is molecularly organized, with SynCAM 1 marking the edge and EphB2 marking the central areas. Third, SynCAM 1 shapes the edge of the cleft. Fourth, SynCAM 1 proteins can form cloud-like ensembles around the postsynaptic border. Fifth, our results support that synaptogenic proteins can undergo activity-dependent re-distribution.

Our cryo-ET analysis provides evidence that the excitatory synaptic cleft can be stratified into layers based on protein densities, reminiscent of the intra-cleft line (Gray, 1959; Hajós, 1980) prominent after phosphotungstic acid staining (Bloom and Aghajanian, 1968). This indicates that clusters of adhesion molecules are repetitively organized. Future studies may uncover effects of maturation stage and brain regions on cleft organization. The density and layer profile of the outer cleft column are shaped by SynCAM 1, consistent with its localization to the postsynaptic edge. We regularly observed synaptic vesicles opposite SynCAM 1-labeled PSD edges and hence consider this zone unlikely to be puncta adhaerentia (Palay, 1967) but rather to be part of synaptic junctions. It is conceivable that SynCAM 1 participates in the conversion of nascent zones, specialized edge regions, into active zones (Bell et al., 2014). The shortened PSDs and active zones in SynCAM 1 KO mice (Robbins et al., 2010) may be due to SynCAM 1 loss in this outer column, consistent with our result that PSDs with SynCAM 1 ensembles are substantially larger than those without.

SynCAM 1 loss and overexpression selectively affect the structural organization of the cleft's edge, supporting that differences in the adhesive makeup of synapses are a factor in shaping them. The central density along the cleft is unaffected by SynCAM 1 and is hence likely established by other proteins such as neuroligins or β-neurexins, which form sheets at non-neuronal cell contacts, with a higher density closer to neuroligin (Tanaka et al., 2012). One reason for the diversity of adhesion systems at excitatory synapses may be that they need to occupy distinct cleft nanodomains to instruct different characteristics of synapses. EphB2, acting during the initial period of synapse formation (Kayser et al., 2008), and SynCAM 1, which induces excitatory synapses and is then required to maintain this increase (Robbins et al., 2010), are differentially localized to areas deeper in the postsynaptic area and around the PSD. The mechanisms that position *trans*-synaptic organizers with such precision are currently unknown. Given the role of SynCAM 1 in synapse maintenance,

it is conceivable that the stabilization of synapses involves interactions at their edge, possibly through links of SynCAM 1 to the postsynaptic cytoskeleton (Cheadle and Biederer, 2012). Selectively positioned *trans*-synaptic proteins may also affect synapse function and define specialized synaptic zones such as proposed for neurotransmitter release (Kavalali, 2015). The density profile of the cleft is relevant for transmission too, because cleft geometry is predicted to shape synaptic currents (Savtchenko and Rusakov, 2007). Moreover, the density of the cleft's edge could control access of extra-synaptic neurotransmitter receptors (Choquet and Triller, 2013) via presentation of binding sites or macromolecular crowding (Santamaria et al., 2010).

PSD size correlates with basal synaptic strength (Harris and Weinberg, 2012), and the presence of SynCAM 1 ensembles linked to larger PSDs may be regulated by the activity history of each synapse. Given the structural dynamics of synapses during plasticity, it is also of interest that postsynaptic SynCAM 1 complexes occupy a larger area after LTD. In contrast to SynCAM 1, neuroligin 1 is rapidly internalized upon LTD (Schapitz et al., 2010) and cleaved (Peixoto et al., 2012). Synapse-organizing proteins hence exhibit distinct activity-dependent dynamics, adding to the molecular diversity of the cleft.

Our study provides evidence that the synaptic cleft is organized into sub-compartments. This introduces the concept of nanodomains to the cleft and expands recent insights into active zones and postsynaptic sites (Choquet and Triller, 2013; MacGillavry et al., 2013; Sigrist and Sabatini, 2012). Differences in the nanoscale organization and dynamics of the cleft may be important parameters that specify synaptic properties.

EXPERIMENTAL PROCEDURES

Tomography

Cerebral cortex homogenates from mice were subjected to differential centrifugation, followed by Percoll gradient purification of synaptosomes and vitrification. Tilt series were collected using a Polara electron microscope (FEI), reconstructed, and segmented.

Immuno-EM

Acute hippocampal slices were prepared, and high-pressure frozen CA1 samples were processed for post-embedding immuno-EM with monoclonal anti-SynCAM 1 antibodies (MBL International, clone 3E1; 1:50). Grids were observed with a FEI Tecnai Biotwin electron microscope.

Neuronal Culture

Hippocampal neurons were cultured from embryonic day 18 rat embryos for STORM imaging and confocal co-localization. Hippocampal cultures from postnatal day 1 rats were used for STED imaging and LTD studies. Chemical LTD was induced at 14 div by treating neurons for 3 min with 20 μM N-methyl-D-aspartate.

Confocal Imaging

Non-permeabilized neurons were subjected at 14 div to surface labeling with antibodies against the extracellular domain of SynCAM 1 (MBL International, 3E1; 1:1,000) or EphB2 (R&D Systems, AF467; 1:100). Homer was immunodetected after permeabilization (Synaptic Systems, 160 003; 1:500), as was PSD-95 (NeuroMab, clone K28/43; 1:500). A Leica TCS SPE DM2500 microscope was used for confocal imaging.

STED Imaging

Neurons were subjected to sequential immunostaining as described above and imaged on a custom-built gated detection, beam scanning, all-pulsed laser STED system with a 100× oil objective (UPLAPO 100XO/PSF, Olympus). Fluorescence was detected by a single photon counting module (SPCM) avalanche photodiode (SPCM-AQR-13-FC, PerkinElmer).

STORM Imaging

Neurons were subjected to sequential immunostaining as described above and imaged on an Olympus IX81 ZDC2 microscope with a 100×/1.49 total internal reflection fluorescence oil objective using simultaneous excitation with 647 and 561 nm lasers. Stochastic blinking was detected with an iXon+ 897 electron microscopy (EM)-charge-coupled device camera (Andor). An astigmatic lens was added, and z axis positions of localized molecules were deduced post hoc.

Statistical Analyses

Data were analyzed using GraphPad Prism 6 and custom ImageJ (confocal) scripts and MATLAB (MathWorks; STED and STORM scripts). *$p < 0.05$; **$p < 0.01$; ***$p < 0.001$.

Animal Procedures

Animal procedures in this study were approved by the Institutional Animal Care and Use Committees, in compliance with NIH guidelines.

SUPPLEMENTAL INFORMATION

Supplemental Information includes Supplemental Experimental Procedures, three figures, and two movies and can be found with this article online at http://dx.doi.org/10.1016/j.neuron.2015.11.011.

AUTHOR CONTRIBUTIONS

K.P.d.A. performed and analyzed EM and confocal imaging and performed STED; N.S. analyzed cryo-ET; S.W.R.M. performed and analyzed STORM; E.A. performed and analyzed STED; G.K.-W.K. recorded cryo-ET; A.-H.T. analyzed STORM; A.J.K. shared mice and supported cryo-ET; V.S. supervised A.J.K.; X.L. supported EM; J.B. supervised E.A.; T.A.B. designed STORM and supervised S.W.R.M. and A.-H.T.; V.L. designed cryo-ET, developed analysis, and supervised N.S. and G.K.-W.K.; and T.B. designed the study with T.A.B. and V.L., supervised K.P.d.A., and wrote the manuscript.

ACKNOWLEDGMENTS

We thank M. Graham for EM support, S. Asano and Z. Kochovski for help with cryo-ET, Dr. D. Lai for script development, Dr. T. Momoi for the SynCAM 1/RA175 KO line, Dr. W. Baumeister for supporting cryo-ET, and Dr. S. Chandra for discussions. We acknowledge support from the Tufts Center for Neuroscience Research under NIH grant P30 NS047243, as well as NIH grants F31 MH105105 (to S.W.R.M.), Wellcome Trust grant 095927/A/11/Z (to J.B.), R01 MH080046 and R01 GM106000 (to T.A.B.), and R01 DA018928 (to T.B.).

Received: March 5, 2015
Revised: September 28, 2015
Accepted: November 5, 2015
Published Date: December 16, 2015

REFERENCES

Bell, M.E., Bourne, J.N., Chirillo, M.A., Mendenhall, J.M., Kuwajima, M., and Harris, K.M. (2014). Dynamics of nascent and active zone ultrastructure as synapses enlarge during long-term potentiation in mature hippocampus. J. Comp. Neurol. *522*, 3861–3884.

Biederer, T., Sara, Y., Mozhayeva, M., Atasoy, D., Liu, X., Kavalali, E.T., and Südhof, T.C. (2002). SynCAM, a synaptic adhesion molecule that drives synapse assembly. Science *297*, 1525–1531.

Bloom, F.E., and Aghajanian, G.K. (1968). Fine structural and cytochemical analysis of the staining of synaptic junctions with phosphotungstic acid. J. Ultrastruct. Res. *22*, 361–375.

Cheadle, L., and Biederer, T. (2012). The novel synaptogenic protein Farp1 links postsynaptic cytoskeletal dynamics and *trans*synaptic organization. J. Cell Biol. *199*, 985–1001.

Choquet, D., and Triller, A. (2013). The dynamic synapse. Neuron *80*, 691–703.

Dani, A., Huang, B., Bergan, J., Dulac, C., and Zhuang, X. (2010). Superresolution imaging of chemical synapses in the brain. Neuron *68*, 843–856.

Elste, A.M., and Benson, D.L. (2006). Structural basis for developmentally regulated changes in cadherin function at synapses. J. Comp. Neurol. *495*, 324–335.

Fogel, A.I., Akins, M.R., Krupp, A.J., Stagi, M., Stein, V., and Biederer, T. (2007). SynCAMs organize synapses through heterophilic adhesion. J. Neurosci. *27*, 12516–12530.

Gray, E.G. (1959). Axo-somatic and axo-dendritic synapses of the cerebral cortex: an electron microscope study. J. Anat. *93*, 420–433.

Hajós, F. (1980). The structure of cleft material in spine synapses of rat cerebral and cerebellar cortices. Cell Tissue Res. *206*, 477–486.

Harris, K.M., and Weinberg, R.J. (2012). Ultrastructure of synapses in the mammalian brain. Cold Spring Harb. Perspect. Biol. *4*, a005587.

High, B., Cole, A.A., Chen, X., and Reese, T.S. (2015). Electron microscopic tomography reveals discrete transcleft elements at excitatory and inhibitory synapses. Front. Synaptic Neurosci. *7*, 9.

Hirano, S., and Takeichi, M. (2012). Cadherins in brain morphogenesis and wiring. Physiol. Rev. *92*, 597–634.

Huang, B., Wang, W., Bates, M., and Zhuang, X. (2008). Three-dimensional super-resolution imaging by stochastic optical reconstruction microscopy. Science *319*, 810–813.

Kavalali, E.T. (2015). The mechanisms and functions of spontaneous neurotransmitter release. Nat. Rev. Neurosci. *16*, 5–16.

Kayser, M.S., Nolt, M.J., and Dalva, M.B. (2008). EphB receptors couple dendritic filopodia motility to synapse formation. Neuron *59*, 56–69.

Lučić, V., Yang, T., Schweikert, G., Förster, F., and Baumeister, W. (2005). Morphological characterization of molecular complexes present in the synaptic cleft. Structure *13*, 423–434.

Lučič, V., Rigort, A., and Baumeister, W. (2013). Cryo-electron tomography: the challenge of doing structural biology in situ. J. Cell Biol. *202*, 407–419.

MacGillavry, H.D., Song, Y., Raghavachari, S., and Blanpied, T.A. (2013). Nanoscale scaffolding domains within the postsynaptic density concentrate synaptic AMPA receptors. Neuron *78*, 615–622.

Missler, M., Südhof, T.C., and Biederer, T. (2012). Synaptic cell adhesion. In Synapses, T.C. Südhof, M. Sheng, and B. Sabatini, eds. (Cold Spring Harbor Laboratory Press), pp. 31–48.

Mortillo, S., Elste, A., Ge, Y., Patil, S.B., Hsiao, K., Huntley, G.W., Davis, R.L., and Benson, D.L. (2012). Compensatory redistribution of neuroligins and N-cadherin following deletion of synaptic β1-integrin. J. Comp. Neurol. *520*, 2041–2052.

Palay, S.L. (1967). Principles of cellular organization in the nervous system. In The Neurosciences, G.C. Quorton, T. Melnchuch, and F.O. Schmitt, eds. (Rockefeller University Press), pp. 24–31.

Peixoto, R.T., Kunz, P.A., Kwon, H., Mabb, A.M., Sabatini, B.L., Philpot, B.D., and Ehlers, M.D. (2012). *Trans*synaptic signaling by activity-dependent cleavage of neuroligin-1. Neuron *76*, 396–409.

Rees, R.P., Bunge, M.B., and Bunge, R.P. (1976). Morphological changes in the neuritic growth cone and target neuron during synaptic junction development in culture. J. Cell Biol. *68*, 240–263.

Robbins, E.M., Krupp, A.J., Perez de Arce, K., Ghosh, A.K., Fogel, A.I., Boucard, A., Südhof, T.C., Stein, V., and Biederer, T. (2010). SynCAM 1 adhesion dynamically regulates synapse number and impacts plasticity and learning. Neuron *68*, 894–906.

Santamaria, F., Gonzalez, J., Augustine, G.J., and Raghavachari, S. (2010). Quantifying the effects of elastic collisions and non-covalent binding on glutamate receptor trafficking in the post-synaptic density. PLoS Comput. Biol. *6*, e1000780.

Savtchenko, L.P., and Rusakov, D.A. (2007). The optimal height of the synaptic cleft. Proc. Natl. Acad. Sci. USA *104*, 1823–1828.

Schapitz, I.U., Behrend, B., Pechmann, Y., Lappe-Siefke, C., Kneussel, S.J., Wallace, K.E., Stempel, A.V., Buck, F., Grant, S.G., Schweizer, M., et al. (2010). Neuroligin 1 is dynamically exchanged at postsynaptic sites. J. Neurosci. *30*, 12733–12744.

Sheffler-Collins, S.I., and Dalva, M.B. (2012). EphBs: an integral link between synaptic function and synaptopathies. Trends Neurosci. *35*, 293–304.

Sigrist, S.J., and Sabatini, B.L. (2012). Optical super-resolution microscopy in neurobiology. Curr. Opin. Neurobiol. *22*, 86–93.

Song, J.Y., Ichtchenko, K., Südhof, T.C., and Brose, N. (1999). Neuroligin 1 is a postsynaptic cell-adhesion molecule of excitatory synapses. Proc. Natl. Acad. Sci. USA *96*, 1100–1105.

Tanaka, H., Miyazaki, N., Matoba, K., Nogi, T., Iwasaki, K., and Takagi, J. (2012). Higher-order architecture of cell adhesion mediated by polymorphic synaptic adhesion molecules neurexin and neuroligin. Cell Rep. *2*, 101–110.

Uchida, N., Honjo, Y., Johnson, K.R., Wheelock, M.J., and Takeichi, M. (1996). The catenin/cadherin adhesion system is localized in synaptic junctions bordering transmitter release zones. J. Cell Biol. *135*, 767–779.

Varoqueaux, F., Jamain, S., and Brose, N. (2004). Neuroligin 2 is exclusively localized to inhibitory synapses. Eur. J. Cell Biol. *83*, 449–456.

Yamagata, M., Herman, J.P., and Sanes, J.R. (1995). Lamina-specific expression of adhesion molecules in developing chick optic tectum. J. Neurosci. *15*, 4556–4571.

Zuber, B., Nikonenko, I., Klauser, P., Muller, D., and Dubochet, J. (2005). The mammalian central nervous synaptic cleft contains a high density of periodically organized complexes. Proc. Natl. Acad. Sci. USA *102*, 19192–19197.

Neuron

Supplemental Information

Topographic Mapping of the Synaptic

Cleft into Adhesive Nanodomains

Karen Perez de Arce, Nikolas Schrod, Sarah W.R. Metzbower, Edward Allgeyer, Geoffrey K.-W. Kong, Ai-Hui Tang, Alexander J. Krupp, Valentin Stein, Xinran Liu, Jörg Bewersdorf, Thomas A. Blanpied, Vladan Lučić, and Thomas Biederer

SUPPLEMENTAL DATA

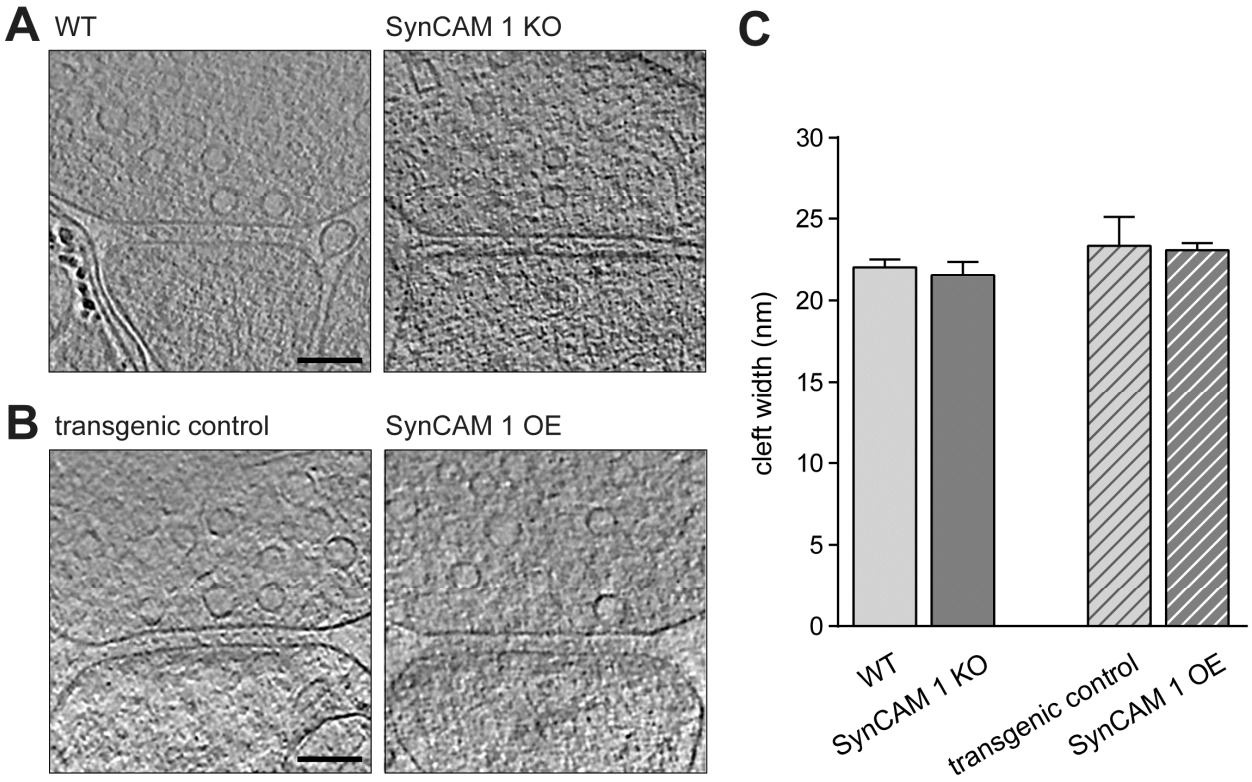

Supplemental Figure S1, related to Figure 1. Cryo-ET imaging and cleft width measurement.

(A) Representative images from tomograms of WT (left) and SynCAM 1 KO (right) synaptosomes. Tomogram data are shown at a depth of 2 voxels (4.6 nm). Scale bar, 100 nm. Note that panels in Figure 2D show tomograms at a depth of 4 voxels to add densities and better visualize cleft differences.

(B) Representative images from tomograms of transgenic control (left) and SynCAM 1 OE (right) synaptosomes. Tomogram data are shown at a depth of 2 voxels (5.5 nm). Scale bar, 100 nm.

(C) Cleft widths were measured in tomograms of synaptosomes from the indicated mouse lines. SynCAM 1 loss in KO mice or overexpression in OE mice did not affect cleft width as compared to littermate controls and across groups (n=7 WT synapses, 8 KO, 5 OE controls, 5 OE).

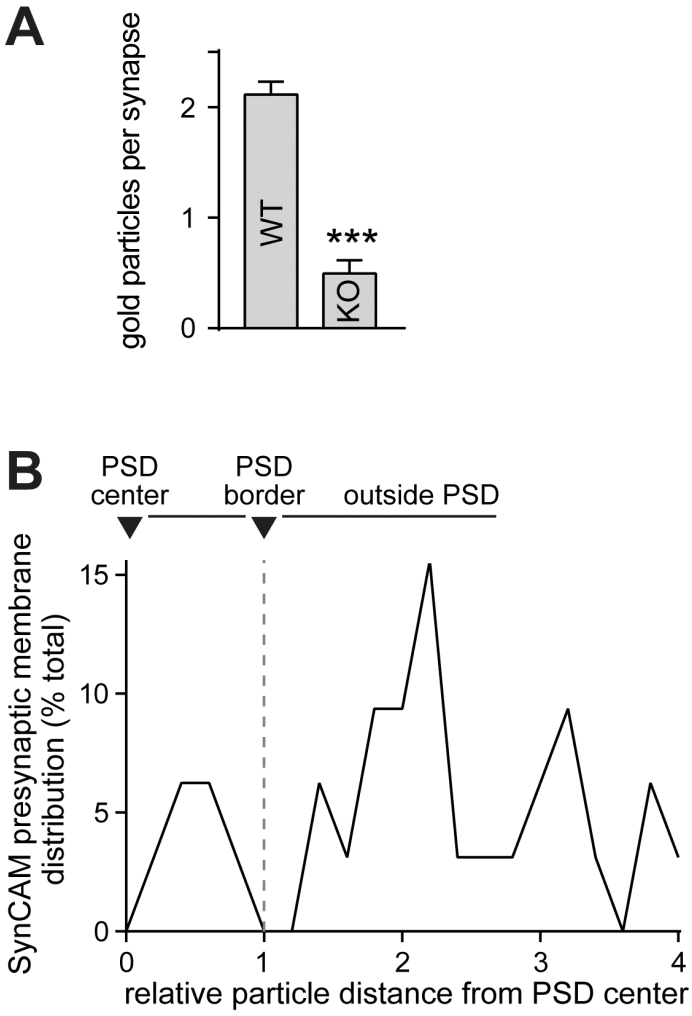

Supplemental Figure S2, related to Figure 2. Specificity of SynCAM 1 immuno-EM detection and protein distribution in presynaptic membranes.

(A) Quantification of gold particles per asymmetric synapse from WT and SynCAM 1 KO sections imaged as in Figure 2A shows specific SynCAM 1 immunolabeling (Mann-Whitney test, $p<0.0001$; N=44 micrographs each).

(B) Distribution of SynCAM 1 particles detected in presynaptic membranes. For each analyzed asymmetric synapse, presynaptic SynCAM 1 particle distances were measured relative to the center of the PSD and normalized to the PSD radius as depicted in Figure 2C, with a value of 1 corresponding to the PSD radius (n=97 micrographs from 3 mice).

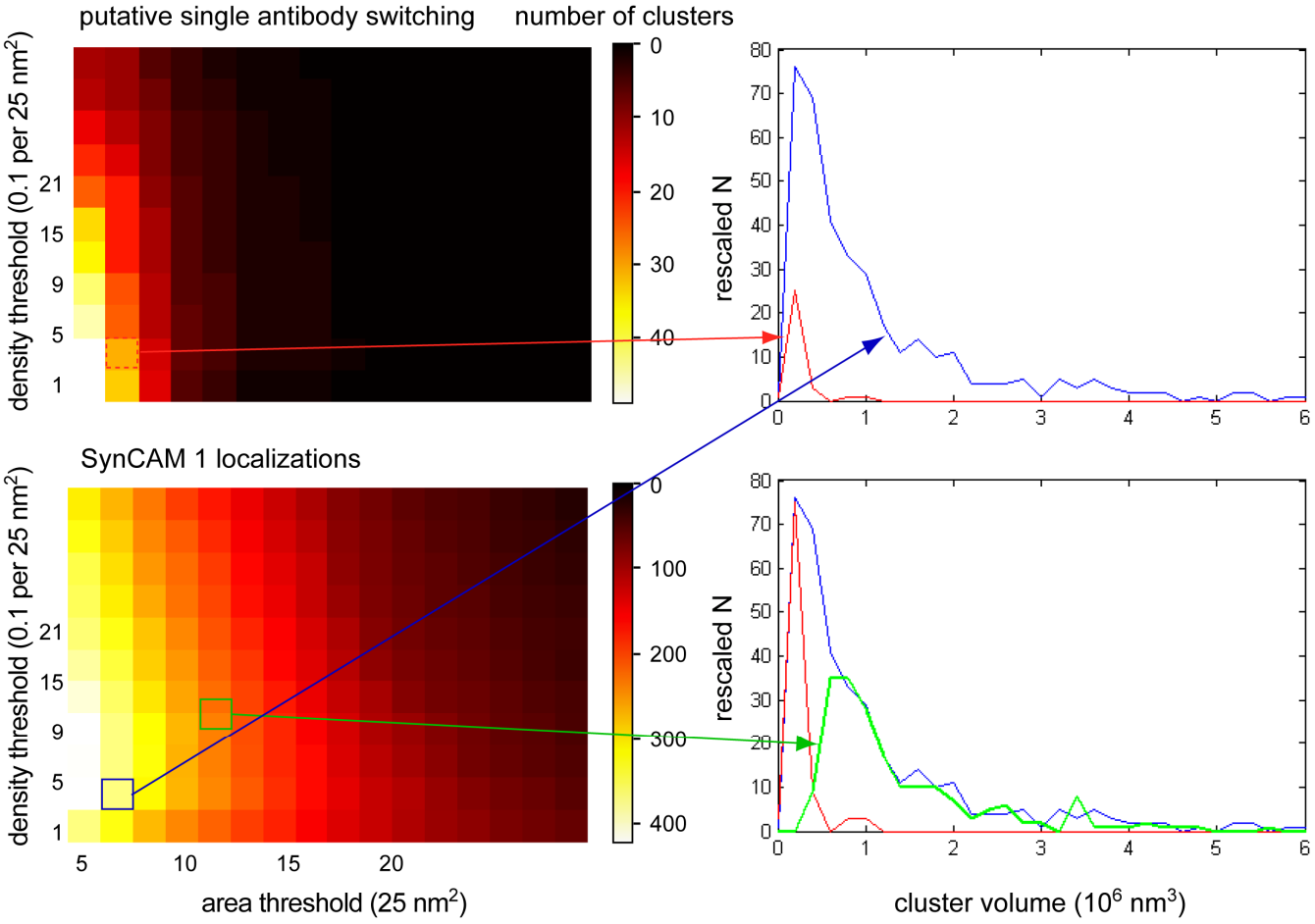

Supplemental Figure S3, related to Figure 3. Approach to identify the borders of SynCAM 1 ensembles.

To develop appropriate criteria for the analysis in Figure 3E, we compared the number of clusters detected with varying thresholds for density and area in each plane (x-y, x-z, and y-z) for the SynCAM 1 STORM data and for PSD-95 staining over a field with no synapses, where all localizations likely arise from repetitive switching of single molecules. In a reconstructed x-y distribution map with a pixel size of 5 nm, at relatively low density and area thresholds (0.3 localizations per pixel and 6 pixels, respectively), there was significant overlap in the distribution of cluster volumes between the SynCAM 1 data and the single molecule data. However, when thresholds were raised to 1 localization per pixel and an area of 10 pixels, single molecule clusters were no longer detected and the distribution of cluster volumes in the SynCAM data showed little overlap with the single molecule cluster volumes detected at the lower threshold (Figure 3E). This suggests that the clusters of SynCAM 1 we measure with these criteria are molecule assemblies of clustered molecules rather than artifacts of imaging or immunostaining.

Supplemental Media File 1, related to Figure 1. 3D cleft representation from a segmented tomogram.
The animation was generated with the Amira program for a 3D representation of the segmented tomogram shown in Figure 1A.

Supplemental Media File 2, related to Figure 1. Composite of a segmented tomogram.
Automated segmentation of a synaptic cleft is shown in red, highlighting the central density closer to the postsynaptic membrane.

SUPPLEMENTAL EXPERIMENTAL PROCEDURES

Synaptosome preparation and vitrification for tomography. Tomography experiments were performed with synaptosomes from SynCAM 1 KO mice (Fujita et al., 2006) generously provided by Dr. T. Momoi (National Institute for Neuroscience, Tokyo) and WT littermate controls in a mixed BL6/129Sv background. In addition, we analyzed SynCAM 1 overexpressor mice carrying the CaMKII-tTA (+/-) x TRE-SynCAM 1 (+/-) transgenes (Robbins et al., 2010) and used single-transgenic CaMKII-tTA (+/-) littermates as controls. These transgenic mice were in a hybrid SV129/Bl6 background. Synaptosomes were prepared as previously described (Dunkley et al., 1988; Godino Mdel et al., 2007). All steps were carried out at 4 °C. Briefly, male mice were sacrificed at 6-9 weeks of age, and the cerebral cortex was extracted and homogenized in ice-cold homogenization buffer (HB; 320 mM sucrose, 50 mM EDTA, 10 mM HEPES at pH 7.4) with up to seven strokes at 700 rpm in a Teflon-glass homogenizer. The homogenate was centrifuged for 2 min at 2,000 × g, the supernatant was centrifuged for 12 min at 9,500 × g, and the resulting pellet was resuspended in HB and loaded onto a three-step (3%, 10%, 23%) Percoll gradient (GE Healthcare). The gradients were spun for 6 min at 25,000 × g, the material accumulated at the 10%/23% interface was recovered and diluted to a final volume of 50 ml in HEPES-buffered medium (HBM, in mM: 140 NaCl, 5 KCl, 5 $NaHCO_3$, 1.2 Na_2HPO_4, 1 $MgCl_2$, 10 glucose, 10 HEPES [pH 7.4]). Percoll was removed by centrifugation for 10 min at 22,000 × g, and the pellet was resuspended in HBM supplemented with 1.2 mM $CaCl_2$. Synaptosomes were vitrified immediately after preparation by plunge-freezing as described (Fernandez-Busnadiego et al., 2013). Briefly, 3 μl of a synaptosomal suspension was placed onto a holey carbon copper electron microscopy grid (Quantifoil) that had been coated with BSA colloidal gold and plunged into a liquid ethane/propane mixture.

Tomographic acquisition, reconstruction and denoising. Tilt series were collected under a low dose acquisition scheme using an electron microscope (Polara; FEI) operated at 300 kV. The microscope was equipped with a field emission gun, a 2,048 × 2,048 charge-coupled device camera (MultiScan; Gatan), a postcolumn energy filter (Gatan) operated in the zero-loss mode, and a computerized cryostage designed to maintain the specimen temperature below -150 °C. Tilt series were recorded using Xplore3D (FEI), typically from -60° to 60° with 1.25°-1.5° angular increment. Pixel size was 0.58-68 nm at the specimen level, and the underfocus was set to 6-7 μm. Tilt series were aligned using gold beads as fiducial markers. 3D reconstructions were obtained by weighted backprojection using EM software (Hegerl, 1996), and tomograms were denoised by anisotropic non-linear diffusion (Fernández and Li, 2003). Tomograms that were not technically good (due to bad alignment or very low signal-to-noise

ratio) as well as those that did not show good structure preservation expected for cryo-preparation (smooth membranes, non-extracted cytosol) were discarded, resulting in total 5-8 tomograms from two mice for each genetic condition. Pre- and post-synaptic membranes were manually segmented in the Amira program. The cleft region was defined as the extracellular region between the membranes that spread as long as the pre- and post-synaptic membranes were parallel to each other. Radial regions (columns) were defined as concentric columns based on the relative position between the center (set to 0) and the cleft edge (set to 1) with bin values of 0, 0.25, 0.5, 0.75 and 1. Four cleft layers were determined by separating the cleft region into four layers of equal thickness parallel to the synaptic membranes. Additional layers of the same thickness were placed on the pre- and post-synaptic membranes to obtain values for normalization. This division into four layers and columns was our resolution limit to detect density differences. Due to the separation into four evenly spaced concentric columns, the outermost column contains approximately the same number of voxels as the inner three.

Tomogram greyscale values are directly related to electron density of the sample, where lower greyscale values correspond to higher densities. To analyze layer profiles, mean greyscale values of all layers in the cleft or for the layers of individual columns were calculated by first finding the individual mean greyscale value of each layer for each synapse, followed by averaging over all synapses of the genetic condition. In the same way, the standard deviation and the standard error of the mean were calculated from the individual means. In order to reduce the greyscale variability between tomograms, the values were shifted so that the mean density of synaptic membranes was set to 0 (Figure 1 E, H). To allow quantitative assessment of differences between layers and columns and the statistical analysis of these differences between genetic conditions, greyscale variability between tomograms arising from the acquisition and reconstruction procedures needed to be eliminated. To achieve this, greyscale values were normalized so that the mean density of synaptic membranes was set to 0 and the mean cleft density to 1 (Figure 1 F, J). This procedure reduces the difference between total cleft values of different tomograms because it leads to an increase of the greyscale values of synapses that contain above-average amount of proteins in the cleft and a decrease for synapses containing below-average amounts. There were no significant differences in synapse size and cleft width between the genetic conditions (Figure S1C). Cleft segmentation was performed using the thresholding and connectivity approach (Lucic et al., 2005). Specifically, clefts were initially segmented by thresholding at a conservative greyscale level and then only the segments that contact both pre- and postsynaptic membranes (in 3D) were selected. Greyscale calculations and the segmentation were done using custom-made software written in Python programming language that uses Numpy and Scipy packages (Oliphant, 2007).

High pressure tissue freezing and immuno-EM labeling. Experiments were performed with tissue from WT and SynCAM 1 KO littermate mice (Fujita et al., 2006) backcrossed for more than 10 generations in a C57Bl/6 background. Because standard pre-embedding immunogold EM did not yield sufficient labeling for quantitative analysis in our studies (data not shown), we employed high-pressure freezing, which improves preservation of proteins on lipids to yield better morphology and higher labeling density (Lonsdale et al., 1999). Acute hippocampal slices were prepared from 3-4 months old mice, allowed to recover for 2 h, and a 2 mm CA1 region was dissected. Unfixed samples were frozen using a Leica HMP101 at 2000 psi and controlled cryoprotecting conditions. Vitrified samples were freeze-substituted using a Leica EM AFS2 unit starting at -90 °C using 0.1% uranyl acetate and 0.125% glutaraldehyde in acetone for 50 hours, rinsed in 100% acetone and infiltrated over 10 hours at -60°C with Lowicryl HM20 resin (Electron Microscopy Science). Samples were placed in gelatin capsules and UV hardened at -50 °C for 8 hours. Blocks were then cut using a Leica UltraCut UC7. 60 nm sections were collected on formvar/carbon coated nickel grids and contrast stained using 2% uranyl acetate and lead citrate.

For immunodetection, the grids were placed section-side down on drops of 0.1 M ammonium chloride to quench untreated aldehyde groups, then blocked for nonspecific binding on 3% albumin from bovine serum (Sigma-Aldrich) in PBS. Single labeled grids were incubated overnight at 4°C on a primary anti-SynCAM 1 monoclonal antibody raised in chicken (MBL International, clone 3E1; 1:50), then bridged for 1 h at RT using rabbit anti-chicken antibodies (Jackson ImmunoResearch) at 1:200, and then incubated for 1 h at RT on anti-rabbit antibody-conjugated 10 nm Protein A gold (10 nm; Utrecht Medical Center) at 1:50. All antibodies and Protein A gold were diluted in PBS containing 3% BSA. The grids were rinsed with PBS, fixed using 1% glutaraldehyde for 5 min, rinsed again, and transferred to a UA/methylcellulose drop before being collected and dried. Grids were observed using a FEI Tecnai Biotwin transmission electron microscope at 80kV accelerating voltage, and images were taken using a SIS Morada CCD camera and iTEM (Olympus) software.

Our post-embedding staining of thin EM sections is expected to allow for uniform antibody access at both the edge and the center of synapses, and access issues are unlikely to cause a detection bias. For quantification of SynCAM 1 distribution across synaptic compartments, presynaptic membranes and terminals were identified by presence of synaptic vesicles within the terminal, and postsynaptic membrane identified due to their association with an electron-dense region. Immunogold particles were only scored as labeling SynCAM 1 in pre- or post-synaptic membranes if particles were within 40 nm of the membrane, using the diameter of the gold particles to approximate this distance. In the few cases when particles were observed within 30 nm from the pre- and post-synaptic membrane, those gold

particles were excluded. Note that the full extracellular domain of a SynCAM dimer has a predicted length of 26-28 nm, assuming that the extracellular domains are rigid and project towards each other (Y. Modis, pers. comm.), and only a small fraction of presynaptic SynCAM 1 closer to the active zone border may connect to SynCAM 1 at the postsynaptic edge.

Neuronal cultures. For STORM analysis, hippocampal neurons were cultured from E18 rat embryos as described (Frost et al., 2010) and plated on cover glasses (MacGillavry et al., 2013).

For confocal microscopy co-localization analysis, hippocampal neurons were prepared from rats at E18 as described (Kaech and Banker, 2006) with modifications. In brief, dissected hippocampi were incubated in 0.05% trypsin at 37 °C for 20 minutes (Invitrogen 25300054) and plated at a density of ~30,000 cells per coverslip. Dissociated cells were plated on poly-l-lysine (Sigma P1274) and incubated in a cell culture incubator with 5.0% CO2. Cytosine arabinoside (Sigma C1768) was added at a final concentration of 2 μM per well 2 days in vitro to prevent glia cell overgrowth.

For confocal microscopy analysis after chemical LTD, primary hippocampal neurons were dissected from rats at P1 as described (Biederer and Scheiffele, 2007) and plated on Matrigel (Becton-Dickinson Biosciences). Chemical LTD was induced by treating neurons at 14 div for 3 min with 20 μM NMDA (Ehlers, 2000; Lee et al., 1998). Medium was then rapidly exchanged, and cultures were incubated for 60 min prior to labeling of surface SynCAM 1 and staining for PSD-95 as described below.

Immunostaining of dissociated neurons for confocal analysis. To measure the extent of triple co-localization of SynCAM 1 and EphB2 together with Homer, surface labeling of EphB2 and SynCAM 1 was performed in neurons at 14 div. Cells were incubated in cold PBS for 3 min to restrict trafficking, followed by 10 min incubation with chicken monoclonal anti-SynCAM 1 (MBL International, clone 3E1; 1:1000) or goat anti-EphB2 (R&D Systems, AF467; 1:100) antibodies against the extracellular domain in PBS. Neurons were kept on ice during antibody surface labeling. After two washes with ice-cold PBS and fixation for 15 min with cold 4% PFA / 4% sucrose in PBS, cells were blocked with 5% FBS in PBS for 1 h at RT, and incubated for 1 h at RT with secondary Alexa-conjugated antibodies (Invitrogen; 1:1000). After washes, cells were permeabilized with 0.1% Triton-X100 in PBS for 10 min at RT, and processed for scaffold protein immunostaining. Homer was detected with antibodies raised in rabbits (Synaptic Systems, 160 003; 1:2000). Mouse monoclonal antibodies detected PSD-95 (NeuroMab, clone K28/43; 1:500). Incubations with secondary Alexa-conjugated antibodies (Invitrogen; 1:1000) were for 1 h at RT. Coverslips were mounted on Aqua-Mount mounting media (Thermo Scientific).

STED imaging. For STED microscopy, hippocampal neurons were prepared from rats at P1 as described (Biederer and Scheiffele, 2007) and plated on 12 mm coverslips #1.5 (Glaswarenfabrik Karl Hecht GmbH&Co KG). At 14 div, SynCAM 1 and EphB2 primary antibody staining was performed under trafficking restrictive conditions as described above. For SynCAM 1, primary antibody surface labeling was followed by incubation with rabbit anti-chicken IgY as bridge antibody (EMD Millipore, 12-334; 1:10,000) for 3 h at 4 °C. After washes, labeling with goat anti-rabbit IgG antibodies conjugated with ATTO-647N (Active Motif, Carlsbad, CA, 15068; 1:500) was performed for 1 h at RT. This was followed by permeabilization and staining for PSD-95 as described above, and detection was performed with goat anti-mouse IgG antibodies (Sigma, 76085; 1:500) labeled with ATTO-594 (ATTO-TEC) for 1 h at RT. For STED microcopy of EphB2, primary antibody labeling was followed by washes and incubation with rabbit anti-goat IgG conjugated with ATTO594 (Abgent, San Diego, CA, ASR1144; 1:250) for 1 h at RT, and extensively washed. This was followed by permeabilization and staining for Homer as described above, and detection was performed with goat anti-rabbit IgG antibodies (Active Motif, Carlsbad, CA, 15068; 1:500) labeled with ATTO-647N (ATTO-TEC) for 1 h at RT. To avoid cross-detection, coverslips were washed extensively after labeling of EphB2 with secondary antibodies prior to Homer detection, and non-overlapping signals were confirmed by confocal and STED microscopy. Coverslips were mounted on Mowiol (Sigma, 81381).

Imaging was performed on a custom built gated detection, beam scanning, all pulsed laser STED system. ATTO-647N conjugated secondary antibodies were imaged by focusing approximately 30 µW (at the back aperture) of picosecond pulsed 650 nm laser light (LDH-P-C-650, Picoquant) into the back aperture of a 100X oil immersion objective lens (UPLAPO 100XO/PSF, Olympus) to excite fluorescence. Similarly, ATTO-594 conjugated secondary antibodies were excited with approximately 35 µW of picosecond pulsed 595 nm excitation light (LDH-TA-595, Picoquant). Fluorescence in the periphery of the excitation spot was depleted with approximately 200 mW of 600 picosecond pulsed 775 nm light (Katana HP, One Five). The depletion light was imprinted with a 2pi phase ramp using a spatial light modulator (X10468, Hamamatsu) and then circularly polarized with a quarter wave plate. Both the depletion and excitation beams were scanned through the sample using a 16 kHz resonant mirror (SC-30, Electro-Optical Products Corp.) and galvanometer mirror pair (DynAXIS XS, ScanLab) conjugated to the objective back pupil plane. Fluorescence was collected by the same objective and separated from the excitation/depletion beam path with a custom dichroic mirror (zt485/595/640/775rpc, Chroma). A second dichroic mirror (zt640rdc, Chroma) separated the ATTO-647N channel from the ATTO-594 channel and each channel employed a set of band pass filters (FF01-685/40 and FF01-624/40, Semrock).

For each channel, fluorescence was focused into a multimode fiber corresponding to approximately 0.8 airy units acting as the confocal pinhole. Finally, fluorescence was detected by a single photon counting avalanche photodiode (SPCM-ARQ-13-FC, Perkin Elmer), collected by an FPGA based data acquisition card (PCIe-7852R, National Instruments), and transferred to a host computer. The excitation and depletion lasers were synchronized with custom electronics (Opsero Electronics) that also hardware gated both detector's signals for gated detection. All images were collected at 10 nm pixel size.

STED image analysis. Image analysis was performed with custom Matlab (Mathworks) scripts. SynCAM 1 or EphB2 spot locations were determined by fitting with a two-dimensional Lorentzian function and their fitted center positions and widths were stored. The corresponding PSD-95 and Homer images, respectively, were analyzed by first lightly blurring with a 1 pixel sigma Gaussian and then setting a threshold of two standard deviations above the mean for all nonzero pixels. This threshold was applied to the original image and size of the remaining regions was examined. Only the top two percent largest regions were retained and their boundaries were determined. In this way, PSD-95 and Homer regions were determined based on size and brightness. Finally, the distance between the center position of each SynCAM 1 spot and the nearest PSD-95 boundary was found. Distances pf EphB2 spots and the nearest Homer boundary were determined in the same way. If a SynCAM 1 or EphB2 spot was found inside a PSD region, the PSD boundary distance was marked as negative. The script is available upon request.

2-Color 3D STORM imaging. Surface labeling of SynCAM 1 and EphB2 followed by staining of intracellular Homer was performed as described above in hippocampal neurons cultured from E18 rats on div 12-14. Secondary anti-chicken antibodies against SynCAM 1 or EphB2, and anti-rabbit antibodies against Homer were conjugated to Cy3 and Alexa 647, respectively. Imaging was performed on an Olympus IX81 ZDC2 inverted microscope with a 100X/1.49 TIRF oil immersion objective. Fluorophores were excited with semi-oblique illumination from 647 nm (100 mW) and 561 nm (150 mW) lasers simultaneously. Stochastic blinking of both molecules was detected with an iXon+ 897 EM-CCD camera (Andor) placed after a 1.6x magnifying optic and a DV2 chromatic image splitter (Photometrics). Frames were acquired at 50 Hz; excitation was pulsed to last 10 ms per frame. A total of 15,000 to 30,000 frames were collected. Hardware was controlled via iQ software (Andor). Z stability was maintained by the Olympus ZDC2 feedback positioning system. An astigmatic lens (f=300 mm) was added to each emission filter holder in the DV2 and the Z-axis positions of localized molecules were deduced post hoc essentially as described (Dani et al., 2010; Huang et al., 2008).

2-Color 3D STORM analysis. All analyses were performed using custom MATLAB (Mathworks) scripts. Molecular positions in the XY plane were estimated by fitting the detected fluorescence peaks with an elliptical 2-D Gaussian function, and Z position was deduced from calibrations of astigmatism above and below the focal plane (Huang et al., 2008; van de Linde et al., 2011). Poorly localized molecules were rejected from the analysis. PSDs were identified based on the density map of Homer localizations analyzed sequentially in the x-y, x-z and y-z planes. Only those clusters that met both density and area criteria were identified as PSDs and used for further analysis. The average density of SynCAM 1 localizations was calculated within 25 nm radial bins from the PSD border by dividing the number of SynCAM 1 localizations by the bin volume. To exclude the effects of PSD shape and optical section restriction, the volume of each bin was deduced by counting the number of uniformly distributed localizations that appeared within it in simulations. The average SynCAM 1 density within the PSD was calculated by dividing the number of SynCAM 1 localizations within the PSD by the total PSD volume defined by Homer localizations. The script is available upon request.

Confocal microscopy and analysis. Confocal imaging was performed on a Leica TCS SPE DM2500 microscope equipped with one spectral PMT. Fluorochromes imaged include Alexa 488, Alexa 594, and Alexa 647 (Invitrogen). Unless otherwise stated, images were acquired with an ACS APO 63x oil lens with 1.3 numerical aperture, using same settings for each condition. The neurite segments that were selected for analysis were between 20-60 μm long. Images were analyzed with ImageJ using scripts custom-written by Ding Lai; Harvard NeuroDiscovery Center Enhanced Neuroimaging Core, Harvard Medical School). The first script measures the extent of immunostaining signal overlap in three channels to determine dual and triple co-localization. The second custom written script measures the area of SynCAM 1 puncta and their distance to the center of the nearest PSD-95 punctum. The scripts are available upon request.

Data and statistical analyses. Data analysis was performed using GraphPad Prism 5 (Graph Pad Software, La Jolla, USA) and MATLAB (Mathworks). * denotes t-test $p<0.05$; ** $p<0.01$; *** $p<0.001$. Data in the text are reported as average ± standard error of the mean. t-tests were unpaired unless noted otherwise in the text.

Animal procedures. All animal procedures undertaken in this study were approved by the Institutional Animal Care and Use Committees and were in compliance with NIH guidelines.

SUPPLEMENTAL REFERENCES

Biederer, T., and Scheiffele, P. (2007). Mixed-culture assays for analyzing neuronal synapse formation. Nature Protocols 2, 670-676.

Dani, A., Huang, B., Bergan, J., Dulac, C., and Zhuang, X. (2010). Superresolution imaging of chemical synapses in the brain. Neuron 68, 843-856.

Dunkley, P.R., Heath, J.W., Harrison, S.M., Jarvie, P.E., Glenfield, P.J., and Rostas, J.A. (1988). A rapid Percoll gradient procedure for isolation of synaptosomes directly from an S1 fraction: homogeneity and morphology of subcellular fractions. Brain Res 441, 59-71.

Ehlers, M.D. (2000). Reinsertion or degradation of AMPA receptors determined by activity-dependent endocytic sorting. Neuron 28, 511-525.

Fernandez-Busnadiego, R., Asano, S., Oprisoreanu, A.M., Sakata, E., Doengi, M., Kochovski, Z., Zurner, M., Stein, V., Schoch, S., Baumeister, W., and Lucic, V. (2013). Cryo-electron tomography reveals a critical role of RIM1alpha in synaptic vesicle tethering. J Cell Biol 201, 725-740.

Fernández, J.J., and Li, S. (2003). An improved algorithm for anisotropic nonlinear diffusion for denoising cryo-tomograms. J Struct Biol 144, 152-161.

Frost, N.A., Shroff, H., Kong, H., Betzig, E., and Blanpied, T.A. (2010). Single-molecule discrimination of discrete perisynaptic and distributed sites of actin filament assembly within dendritic spines. Neuron 67, 86-99.

Fujita, E., Kouroku, Y., Ozeki, S., Tanabe, Y., Toyama, Y., Maekawa, M., Kojima, N., Senoo, H., Toshimori, K., and Momoi, T. (2006). Oligo-astheno-teratozoospermia in mice lacking RA175/TSLC1/SynCAM/ IGSF4A, a cell adhesion molecule in the immunoglobulin superfamily. Mol Cell Biol 26, 718-726.

Godino Mdel, C., Torres, M., and Sanchez-Prieto, J. (2007). CB1 receptors diminish both Ca(2+) influx and glutamate release through two different mechanisms active in distinct populations of cerebrocortical nerve terminals. J Neurochem 101, 1471-1482.

Hegerl, R. (1996). The EM program package: A platform for image processing in biological electron microscopy. J Struct Biol 116, 30-34.

Huang, B., Wang, W., Bates, M., and Zhuang, X. (2008). Three-dimensional super-resolution imaging by stochastic optical reconstruction microscopy. Science 319, 810-813.

Kaech, S., and Banker, G. (2006). Culturing hippocampal neurons. Nat Protoc 1, 2406-2415.

Lee, H.K., Kameyama, K., Huganir, R.L., and Bear, M.F. (1998). NMDA induces long-term synaptic depression and dephosphorylation of the GluR1 subunit of AMPA receptors in hippocampus. Neuron 21, 1151-1162.

Lonsdale, J.E., McDonald, K.L., and Jone, R.L. (1999). High pressure freezing and freeze substitution reveal new aspects of fine structure and maintain protein antigenicity in barley aleurone cells. The Plant Journal 17, 221-229.

Lucic, V., Forster, F., and Baumeister, W. (2005). Structural studies by electron tomography: from cells to molecules. Annu Rev Biochem 74, 833-865.

MacGillavry, H.D., Song, Y., Raghavachari, S., and Blanpied, T.A. (2013). Nanoscale scaffolding domains within the postsynaptic density concentrate synaptic AMPA receptors. Neuron 78, 615-622.

Oliphant, T.E. (2007). Python for Scientific Computing. Comp Sci & Eng 9, 10-20.

Robbins, E.M., Krupp, A.J., Perez de Arce, K., Ghosh, A.K., Fogel, A.I., Boucard, A., Sudhof, T.C., Stein, V., and Biederer, T. (2010). SynCAM 1 adhesion dynamically regulates synapse number and impacts plasticity and learning. Neuron 68, 894-906.

van de Linde, S., Loschberger, A., Klein, T., Heidbreder, M., Wolter, S., Heilemann, M., and Sauer, M. (2011). Direct stochastic optical reconstruction microscopy with standard fluorescent probes. Nat Protoc 6, 991-1009.

1

Topographic Mapping of the Synaptic Cleft into Adhesive Nanodomains.

Perez de Arce K, Schrod N, Metzbower SW, Allgeyer E, Kong GK, Tang AH, Krupp AJ, Stein V, Liu X, Bewersdorf J, Blanpied TA, Lucić V, Biederer T
show author affiliations

Neuron. 2015 Dec 16; 88(6):1165-72

Recommendations:

Good 10 Jun 2016

FM Donna Webb
F1000 Cell Biology
Vanderbilt University, Nashville, TN, USA.

NEW FINDING

DOI: 10.3410/f.726027954.793519388

The advent of super resolution imaging has revolutionized the study of spines and synapses. Super resolution microscopy has also been used to visualize protein nanodomains within both the postsynaptic density (PSD) and other areas of the spine. Different individual nanodomains of the same protein display different life times and changes in morphology over time. Less clear, though, is how protein nanodomains are established during neuronal development and how they change over time in response to synaptic plasticity. Interestingly, this study showed that synaptic cell adhesion molecule 1 (SynCAM 1), a protein involved in synapse organization, displayed an increase in nanodomain size in response to long-term depression. Collectively, this finding, together with those of {1,2}, indicates that changes to nanodomain composition and characteristics are key for altering synaptic strength and suggests that changes to nanodomain composition occur during different stages of spine development.

This Recommendation is of an article referenced in an F1000 Faculty Review also written by Cristina M. Robinson, Mikin R. Patel, and Donna J. Webb.

References

1. **Multiple spatial and kinetic subpopulations of CaMKII in spines and dendrites as resolved by single-molecule tracking PALM.**
Lu HE, MacGillavry HD, Frost NA, Blanpied TA. J Neurosci. 2014 May 28; 34(22):7600-10
PMID: 24872564 DOI: 10.1523/JNEUROSCI.4364-13.2014

2. **Psychiatric risk factor ANK3/ankyrin-G nanodomains regulate the structure and function of glutamatergic synapses.**
Smith KR, Kopeikina KJ, Fawcett-Patel JM, Leaderbrand K, Gao R, Schürmann B, Myczek K, Radulovic J, Swanson GT, Penzes P. Neuron. 2014 Oct 22; 84(2):399-415
PMID: 25374361 DOI: 10.1016/j.neuron.2014.10.010